Soft Science

Supplementary Materials

Bead-on-string Ag/AgCl heterostructures enable nonpolarizable stretchable dry electrodes for long-term, high-fidelity electrophysiological interfaces

Hengyuan Shang[1,#], Jiangtao Li[1,#], Beibei Shao[1,*], Bo Shi[1], Yuqi Liu[1], Teng Gao[1], Yuxuan Li[1], Yanyun Liu[1], Le Jen Huang[2], Wenzhe Chen[2], Tao Song[1,*], Baoquan Sun[1,3,*]

[1]State Key Laboratory of Bioinspired Interfacial Materials Science, Institute of Functional Nano & Soft Materials (FUNSOM), Soochow University, Suzhou 215123, Jiangsu, China.
[2]Tripod (Wuxi) Electronic Co., Ltd., Wuxi 214000, Jiangsu, China.
[3]Macau Institute of Materials Science and Engineering, MUST-SUDA Joint Research Center for Advanced Functional Materials, Macau University of Science and Technology, Macau 999078, China.
[#]These authors contributed equally to this work.

[*]**Correspondence to:** Prof. Beibei Shao, Prof. Tao Song, Prof. Baoquan Sun, State Key Laboratory of Bioinspired Interfacial Materials Science, Institute of Functional Nano & Soft Materials (FUNSOM), Soochow University, Suzhou 215123, Jiangsu, China. E-mail: bbshao@suda.edu.cn; tsong@suda.edu.cn; bqsun@suda.edu.cn

Supplementary Tables

Supplementary Table 1. Representative reported dry electrodes and their physical properties

Electrode	Sheet resistance (Ω sq^{-1})	Stretchability (%)	Impedance at 10 Hz (kΩ)	Ref.
PEG-CTH/AgNWs	4.95	122	316	[1]
SEBS/Silbione/AgNWs	0.78	406	100	[2]
PEDOT:PSS/PVA/AgNWs/PU	3.90	100	60	[3]
PDMS/AgNWs	0.48	70	1000	[4]
BAP/AgNWs	0.47	697	304	[5]
NFM/AgNWs	1.47	160	200	[6]
SESA/CNT	134	600	158	[7]
PEDOT:PSS/EG/Maltitol	140	62	126	[8]
AgNWs/AgCl/SEBS	0.43	400	49	This work

Supplementary Table 2. HSP of the components. The values for SEBS and PVP-Ag were calculated *via* the group contribution method

Component	δ_D	δ_P	δ_H	R_0
PVP-Ag	19.8	12.1	14.7	13.4
SEBS	16.9	0.6	1.1	4.5
Toluene	18.0	1.4	2.0	-
Ethanol	15.8	8.8	19.4	-

All calculations were performed using HSPiP software.

Supplementary Table 3. HSP values of the binary solvent system at 25 °C

Ethanol: Toluene (*v/v*)	δ_D	δ_P	δ_H
1:10	17.8	2.1	3.7
1:5	17.6	2.6	4.9
1:2.5	17.4	3.5	7.0
1:1	16.9	5.1	10.7

Calculated using the HSPiP software.

Supplementary Table 4. Impedance fitting results for the various electrodes

Sample	R_{sub} (Ω)	R_s (Ω)	C_s (F)	R_{ct} (Ω)	C_{dc} (F)
AS	139.2	10766	1.0596×10^{-7}	251830	3.5754×10^{-7}
25 wt%	188.9	9374	6.9559×10^{-7}	93420	9.6682×10^{-7}
40 wt%	196.1	6335	5.9362×10^{-7}	44933	1.5925×10^{-6}
50 wt%	171.2	6855	7.0346×10^{-7}	56376	1.5614×10^{-6}

Supplementary Figures

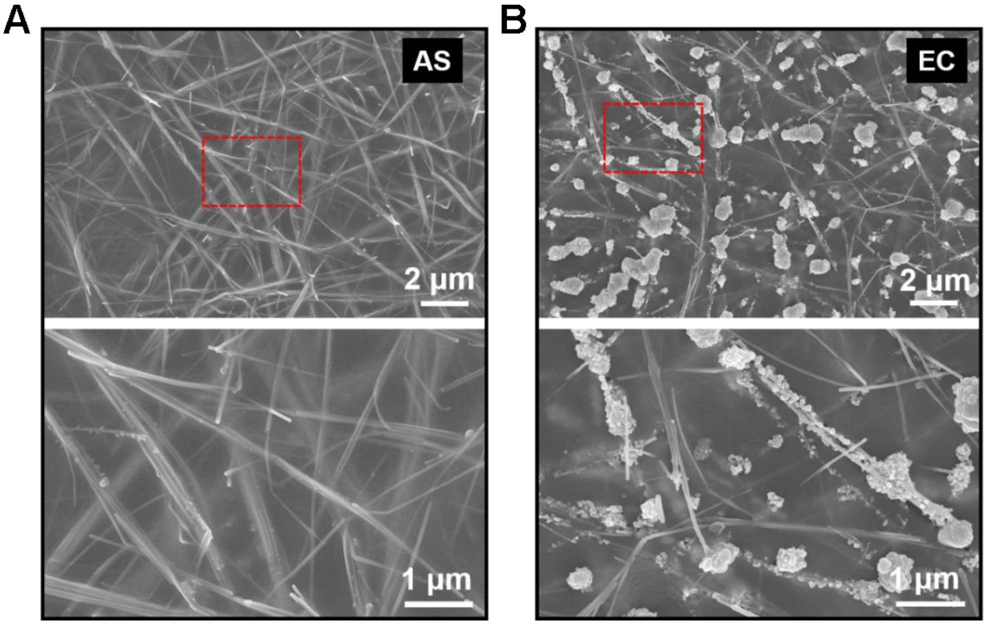

Supplementary Figure 1. SEM images of (A) AS and (B) EC films. After electrochemical chlorination, AgCl is in situ formed on the AgNWs.

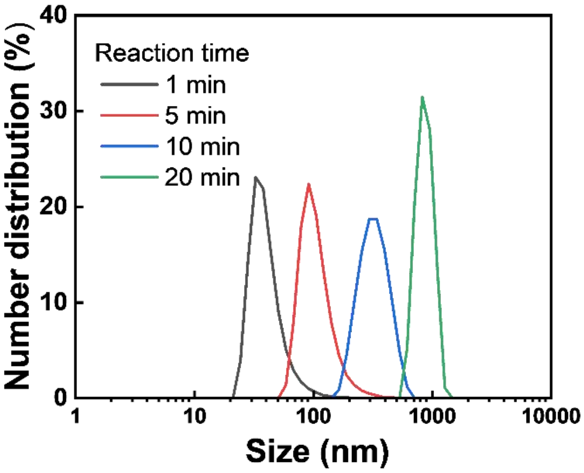

Supplementary Figure 2. Particle size distributions of AgCl NPs obtained at different reaction times. The sizes were determined by a dynamic light scattering method.

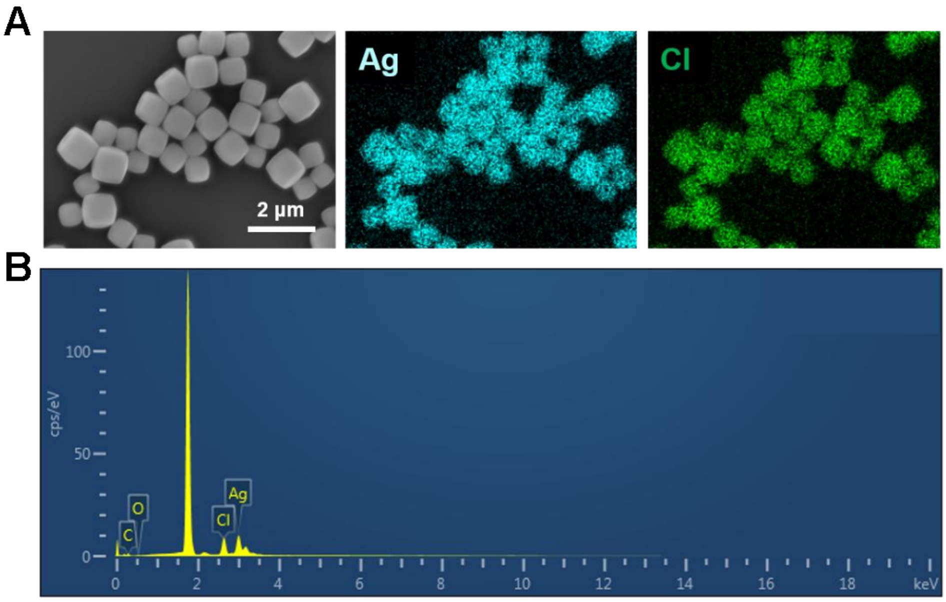

Supplementary Figure 3. Morphology and elemental characterization of AgCl particles. (A) SEM/EDS images of AgCl NPs. (B) The Ag:Cl atomic ratio is approximately 1:1, indicating that excess Cl^- remained in the reaction solution and was removed during purification. C and O are from PVP ligands.

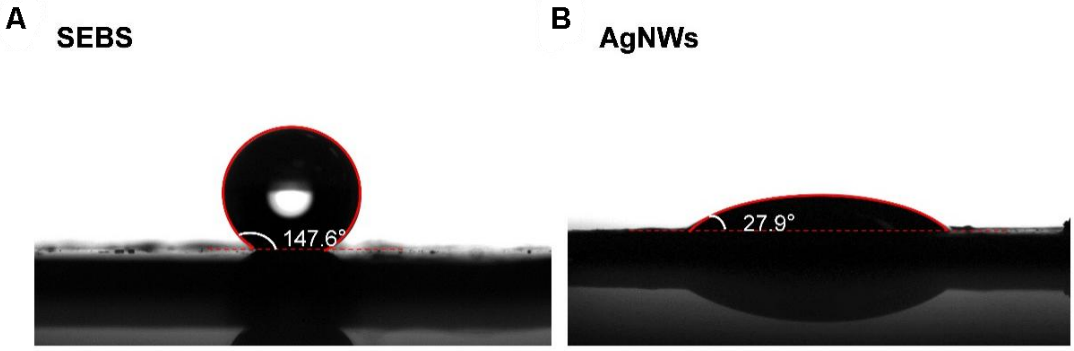

Supplementary Figure 4. Water contact angle measurement of (A) SEBS and (B) AgNWs. There is a significant difference in their surface energies.

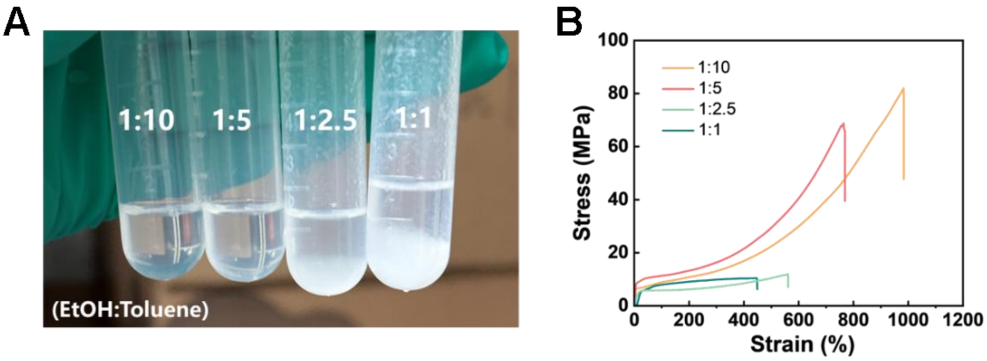

Supplementary Figure 5. Experimental validation of the HSP space. (A) Dissolution behavior of SEBS in ethanol/toluene mixtures with different volume ratios. Solvent compositions located outside the SEBS solubility sphere induce partial precipitation of SEBS. Photographs were taken by the authors. (B) Stress-strain curves of pristine SEBS films after solvent evaporation. The solubility of SEBS in the solvent mixture strongly affects its maximum elongation at break.

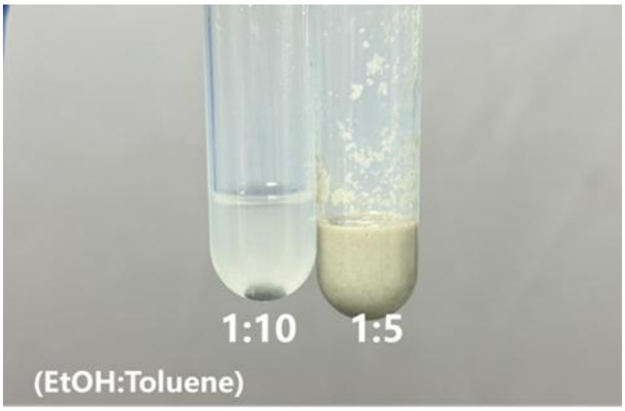

Supplementary Figure 6. Photographs of the AAS precursor solutions prepared with different solvent ratios. An ethanol/toluene ratio of 1:10 leads to phase separation of the inorganic component, whereas a 1:5 ratio enables the formation of a uniform, stable dispersion. Photographs were taken by the authors.

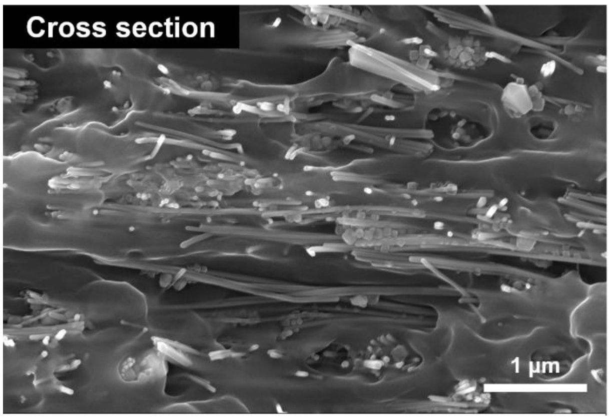

Supplementary Figure 7. Cross-sectional SEM image of the AAS electrode.

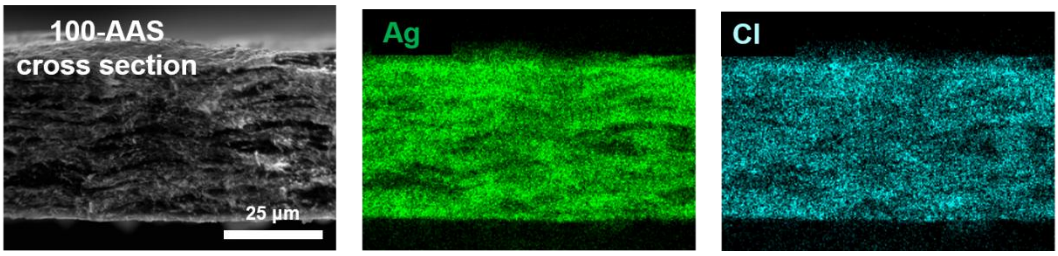

Supplementary Figure 8. Cross-sectional SEM/EDS images of the AAS electrode, showing that AgCl NPs are uniformly distributed throughout the film interior.

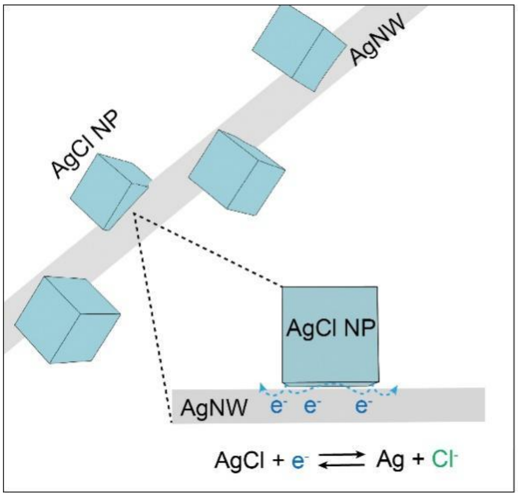

Supplementary Figure 9. Schematic illustration of the proposed interaction mechanism between AgCl NPs and AgNWs within the AAS electrode. The enlarged inset illustrates the proposed interfacial electronic coupling and reversible redox process at the Ag/AgCl interface.

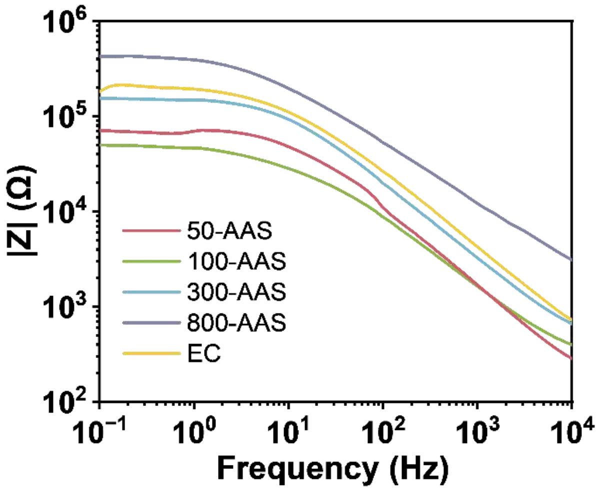

Supplementary Figure 10. Skin-electrode contact impedance of AAS electrodes based on AgCl NPs with different sizes and EC electrode.

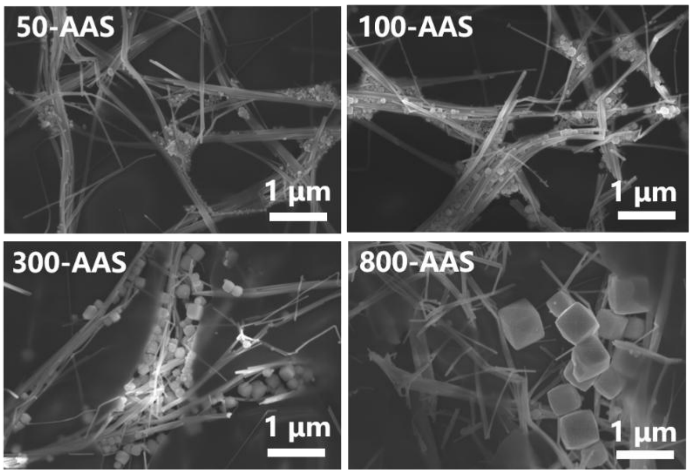

Supplementary Figure 11. SEM images of stretched AAS electrodes based on AgCl NPs with different sizes.

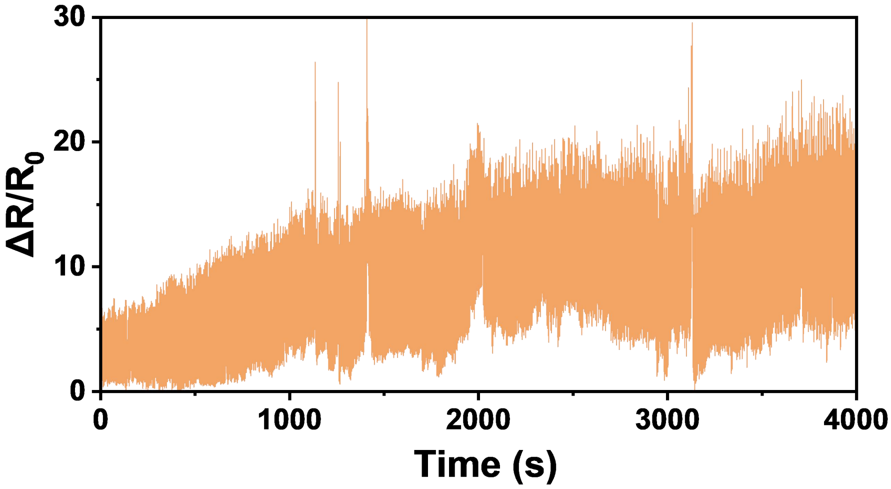

Supplementary Figure 12. Resistance changes of the EC electrode at 0-100% strain during 500 stretching cycles.

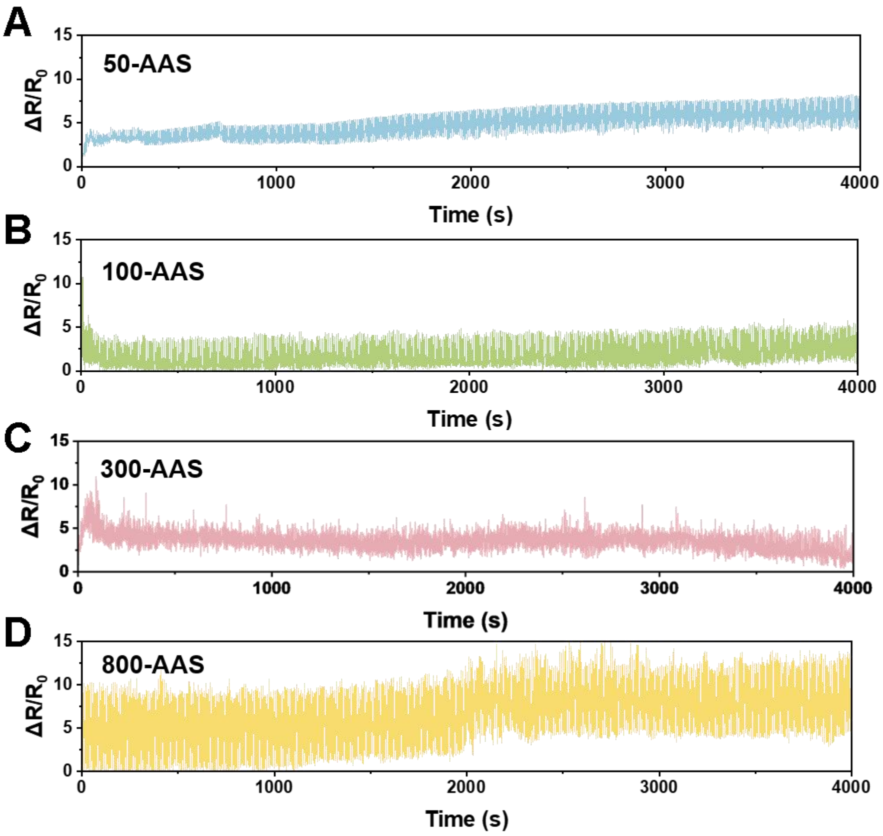

Supplementary Figure 13. Resistance changes of AAS electrodes with AgCl NPs of different sizes at 0-100% strain during 500 stretching cycles: (A) 50-AAS, (B) 100-AAS, (C) 300-AAS, and (D) 800-AAS.

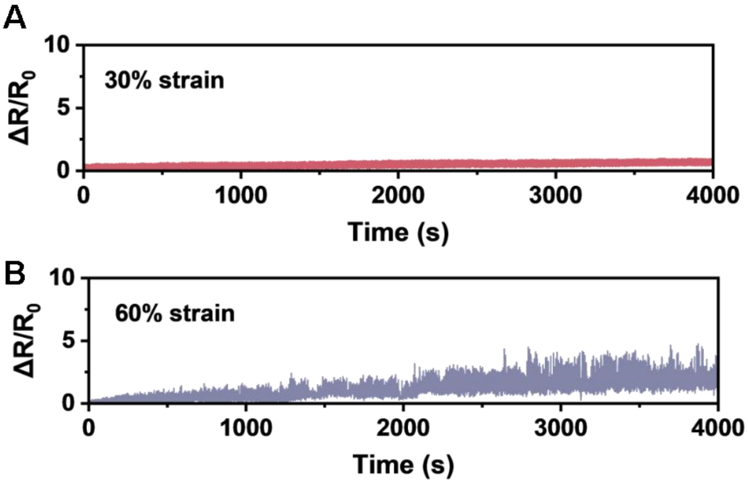

Supplementary Figure 14. Resistance changes of 100-AAS electrodes with (A) 30% strain and (B) 60% strain during 500 cyclic stretching cycles.

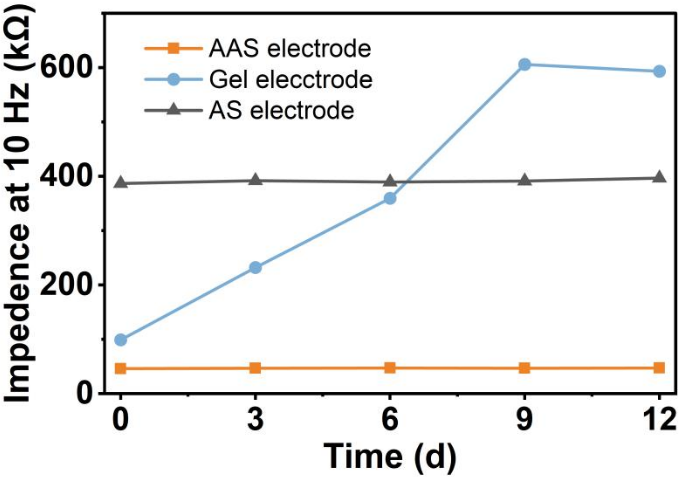

Supplementary Figure 15. Variation of skin-electrode contact impedance using the AS electrode, commercial gel electrode, and the AAS electrode after 12 days of storage in air.

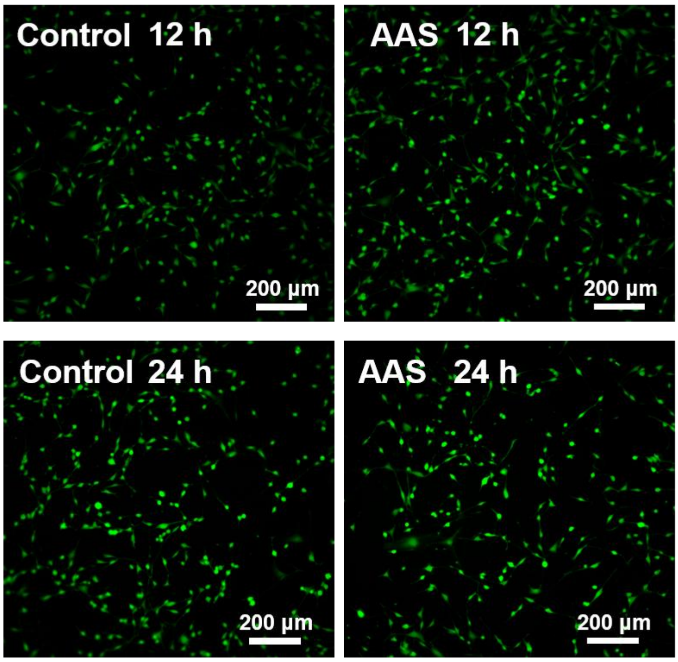

Supplementary Figure 16. Fluorescent images of stained NIH/3T3 cells cultured on the solvent control group and the AAS electrode after 12h and 24 h. Live cells: green. Dead cells: red.

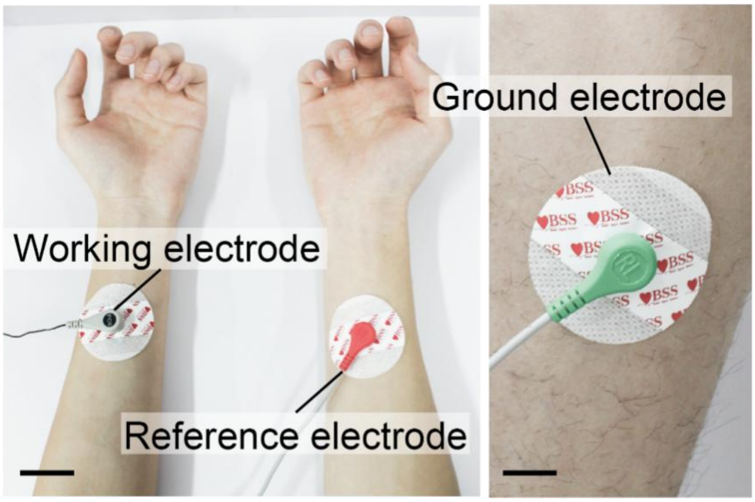

Supplementary Figure 17. Photographs of electrode placement during ECG recording. The ground electrode was placed on the subject's lower leg. Scale bar: 5 cm (left) and 2 cm (right). Photographs were taken by the authors.

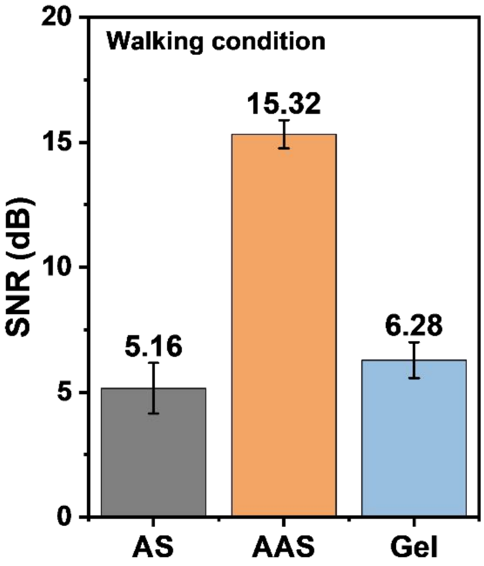

Supplementary Figure 18. SNR values of ECG signals acquired under walking conditions using the AS electrode, commercial gel electrode, and the AAS electrode. The error bars indicate the SD obtained from repeated tests (n=5).

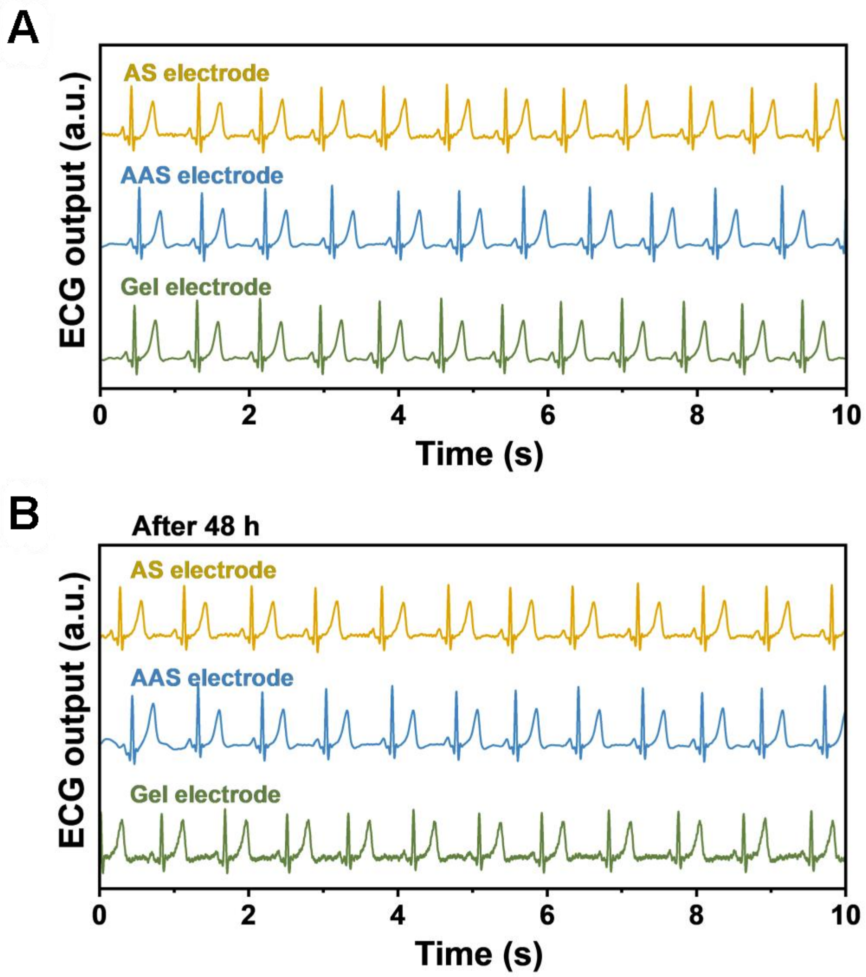

Supplementary Figure 19. (A) ECG recordings acquired using the AS electrode, commercial gel electrode, and the AAS electrode under identical measurement conditions. (B) ECG recordings obtained with the three types of electrodes after 48 h of storage in air.

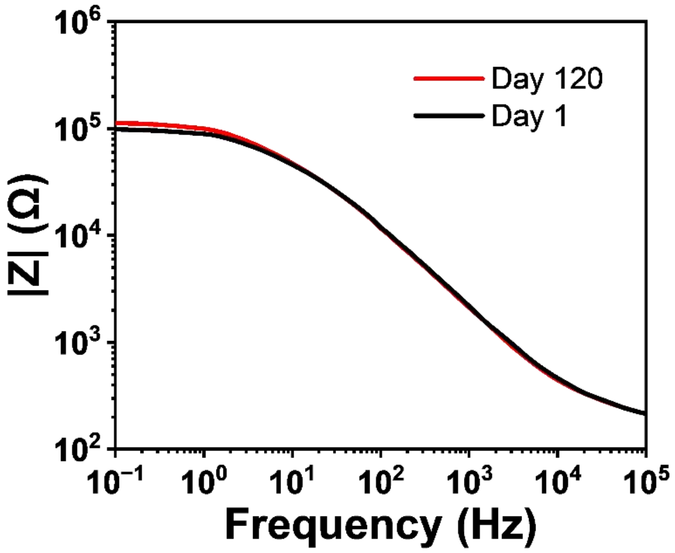

Supplementary Figure 20. Skin-electrode contact impedance of the AAS electrode after 120 days of storage in air, showing only a slight increase compared with the initial value.

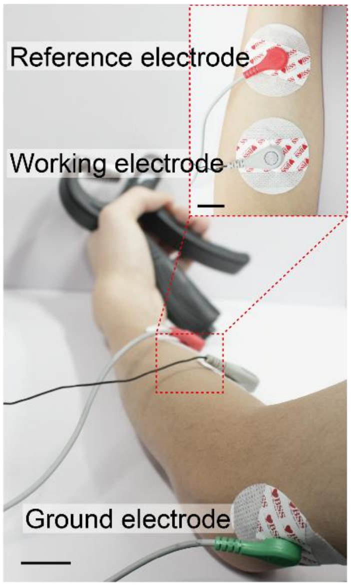

Supplementary Figure 21. Photographs of electrode placement during EMG recording. Scale bar: 5cm; inset: 2 cm. Photographs were taken by the authors.

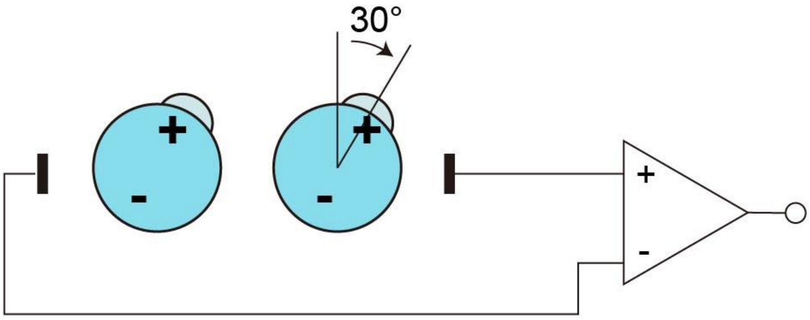

Supplementary Figure 22. EOG recording mechanism. EOG reflects the potential difference between the retina and the cornea of human eyes, which can be modeled as a dipole with a positive potential on the cornea and a negative potential on the retina[9].

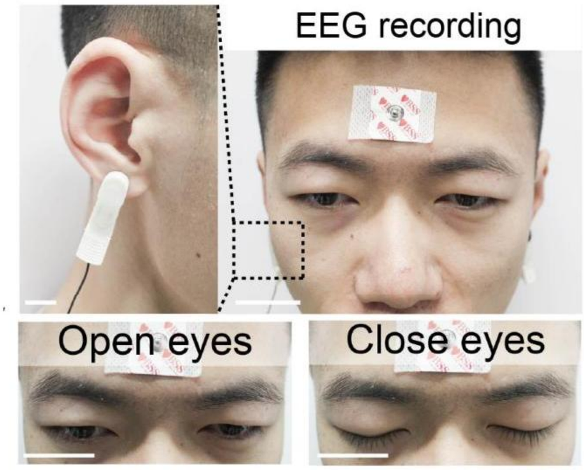

Supplementary Figure 23. Photographs of electrode placement during EEG recording. Scale bar: 3 cm; enlarge: 2 cm. Photographs were taken by the authors. Written informed consent for publication of the photograph was obtained from the participant.

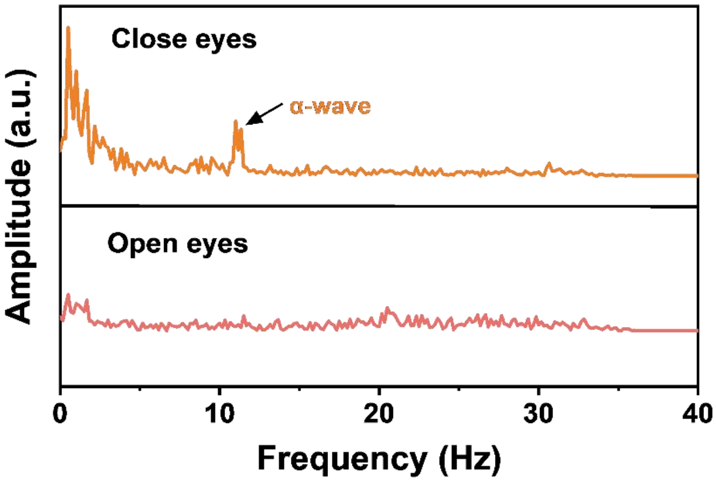

Supplementary Figure 24. Frequency-domain spectra during EEG recording.

REFERENCES

1. Wang, J.; Zhai, B.; Zhang, J.; et al. Stretchable, breathable and skin-conformal nanofilm-based epidermal dry electrodes for electrophysiological and motion monitoring. *Adv. Funct. Mater.* **2026**, e24980. DOI: https://doi.org/10.1002/adfm.202524980
2. Li, J.; Zhang, S.; Zhong, J.; et al. Laser-induced graphene-assisted patterning and transfer of silver nanowires for ultra-conformal breathable epidermal electrodes in long-term electrophysiological monitoring. *Adv. Funct. Mater.* **2025**, *35*, 2504481. DOI: https://doi.org/10.1002/adfm.202504481
3. Xia, M.; Liu, J.; Kim, B.J.; et al. Kirigami-structured, low-impedance, and skin-conformal electronics for long-term biopotential monitoring and human-machine interfaces. *Adv. Sci.* **2024**, *11*, 2304871. DOI: https://doi.org/10.1002/advs.202304871
4. Zou, X.; Xue, J.; Li, X.; et al. High-fidelity sEMG signals recorded by an on-skin electrode based on AgNWs for hand gesture classification using machine learning. *ACS Appl. Mater. Interfaces* **2023**, *15*, 19374-19383. DOI: https://doi.org/10.1021/acsami.2c21354
5. Lai, H.; Liu, Y.; Cheng, Y.; Shi, L.; Wang, R.; Sun, J. Temperature-triggered adhesive bioelectric electrodes with long-term dynamic stability and reusability. *Adv. Sci.* **2023**, *10*, 2300793. DOI: https://doi.org/10.1002/advs.202300793
6. Zhu, M.; Xu, W.; Chen, L.; et al. Ultrathin self-healing nanofibrous membrane with a hierarchical confined structure for biomimetic epidermal electrodes. *ACS Nano* **2024**, *18*, 28834-28848. DOI: https://doi.org/10.1021/acsnano.4c08617
7. Cheng, Y.; Zhou, Y.; Wang, R.; et al. An elastic and damage-tolerant dry epidermal patch with robust skin adhesion for bioelectronic interfacing. *ACS Nano* **2022**, *16*, 18608-18620. DOI: https://doi.org/10.1021/acsnano.2c07097
8. Lin, X.; Ou, Z.; Wang, X.; et al. Self-adhesive and biocompatible dry electrodes with conformal contact to skin for epidermal electrophysiology. *Interdiscip. Mater.* **2024**, *3*, 775-790. DOI: https://doi.org/10.1002/idm2.12198
9. Ameri, S.K.; Kim, M.; Kuang, I.A.; et al. Imperceptible electrooculography graphene sensor system for human-robot interface. *npj 2D Mater. Appl.* **2018**, *2*, 19. DOI: https://doi.org/10.1038/s41699-018-0064-4